



**HAL**  
open science

## Low-cost WO<sub>3</sub> nanoparticles / PVA smart photochromic glass windows for sustainable building energy savings

Yazan Badour, Sylvain Danto, Subhy Albakour, Stephane Mornet, Nicolas Penin, Lionel Hirsch, Manuel Gaudon

### ► To cite this version:

Yazan Badour, Sylvain Danto, Subhy Albakour, Stephane Mornet, Nicolas Penin, et al.. Low-cost WO<sub>3</sub> nanoparticles / PVA smart photochromic glass windows for sustainable building energy savings. Solar Energy Materials and Solar Cells, 2023, 255, 112291 (11 p.). 10.1016/j.solmat.2023.112291 . hal-04050807

**HAL Id: hal-04050807**

**<https://hal.science/hal-04050807v1>**

Submitted on 29 Mar 2023

**HAL** is a multi-disciplinary open access archive for the deposit and dissemination of scientific research documents, whether they are published or not. The documents may come from teaching and research institutions in France or abroad, or from public or private research centers.

L'archive ouverte pluridisciplinaire **HAL**, est destinée au dépôt et à la diffusion de documents scientifiques de niveau recherche, publiés ou non, émanant des établissements d'enseignement et de recherche français ou étrangers, des laboratoires publics ou privés.

**Low-cost WO<sub>3</sub> nanoparticles / PVA smart photochromic glass windows for sustainable building energy savings**

**Yazan Badour<sup>1</sup>, Sylvain Danto<sup>1</sup>, Subhy Albakour<sup>2</sup>, Stephane Mornet<sup>1</sup>, Nicolas Penin<sup>1</sup>, Lionel Hirsch<sup>3</sup>, Manuel Gaudon<sup>1\*</sup>**

<sup>1</sup> CNRS, Univ. Bordeaux, Bordeaux INP, ICMCB (UMR 5026), Pessac F-33600, France

<sup>2</sup> Institut Polytechnique de Paris (IP Paris), 91120 Palaiseau, France.

<sup>3</sup> CNRS, Univ. Bordeaux, Bordeaux INP, IMS, (UMR 5218), Talence F-33400, France,

\* corresponding author: manuel.gaudon@icmcb.cnrs.fr

**Abstract**

In this paper, we investigate the WO<sub>3-x</sub>/PVA composite films as smart photochromic coatings on glass substrate by two methods: solvent casting (SC) and dip-coating (DC). The two methods were thoroughly compared using experimental and theoretical means. All prepared films have been optically investigated by *ex-situ* and *in-situ* UV-Vis spectrometry, leading to insight on their coloring/bleaching amplitudes and kinetics. It was found that the SC films exhibited the best photochromic amplitude with a visible and infrared optical contrast  $\Delta C_{\text{vis}} = 34.37$  and  $\Delta C_{\text{IR}} = 7.9$ , whereas  $\Delta C_{\text{vis}}$  and  $\Delta C_{\text{IR}}$  reached less than 20.2 and 5.4 for the best films issued from the DC process. Further, a two-flux model (KubelkaMunk) was adapted to understand the associated impacts of absorption and scattering in our composite films. The calculations revealed that the simulated scattering factor was higher in the case of the DC films than for the SC films, explaining hence the higher photochromic amplitude of the latter. After carefully analyzing the relationship between the SC and DC films characterizations and optical performance, we concluded that the SC method offered films that are a better candidate for post-optical

application in terms of scattering reduction, improved visible/infrared contrast, and better photochromic efficiency. Nevertheless, the “thick” SC films get a slightly lower kinetic response than the “thin” DC films. Finally, the cooling effect of the photochromic SC films was tested by integrating them in a model wooden room under the irradiation of an artificial solar source. The photochromic SC smart windows proposed here are equally efficient while being more affordable than electrochromic panels or VO<sub>2</sub> thermochromic thin films to reduce the inner house temperature (almost 20°C) upon solar irradiation, demonstrating their great potential as smart cost-effective energy-saving materials

**Keywords:** Smart window; Photochromic window; Tungsten oxide; Energy saving materials; Thermal insulation.

## **1- Introduction**

Energy saving is a major factor in the sustainable development of our society, especially in the context of forthcoming restricted global energy resources [1]. Bearing in mind the accelerating increase of pollution and consumption of fossil energy resources, the need for new energy concepts is essential for our future society [2]. Buildings account for approximately 40% of the energy consumption and 36% of the CO<sub>2</sub> emissions (in the EU) [2,3]. Approximately 60% of the energy consumed in buildings is lost through inefficient windows systems. In this context, the transparent windows of the buildings must better act as a thermal barrier between the internal and external environments which can reduce the requirements for air conditioning and lighting energy consumption [3]. Eco-design of buildings is the solution for both new construction and existing buildings renovation, which can be achieved by using smart window systems. This type

of windows can continuously and automatically change energy and light transmission values with external environmental conditions [1,3,4]. One well-known class of smart windows is chromogenic windows. Chromogenic materials can change their optical appearance reversibly in response to an external stimulus. There are different types of chromogenic materials including photochromic [5], thermochromic [4], gas-chromic, and electrochromic materials [5,6]. In the goal of achieving energy-efficient materials, tungsten oxide ( $\text{WO}_{3-x}$ ) based smart coatings have gained much attention in recent years due to their variety of structures and promising application such as photochromic optical devices, gas sensors, photocatalysts, flat panel displays, and solar filters [6]. Tungsten oxide is the most widely studied inorganic photochromic oxide [7] since discovery of the photochromic phenomenon in 1966 [8,9]. The control of composition (as doping ions can be added [10]), structure (hexagonal versus monoclinic forms [10,11] and morphologies and sizes (with the best results obtained on highly divided  $\text{WO}_3$  [12]) both impact the light response amplitude and speed. Nevertheless, some challenges still exist; especially, the long bleaching time (at least several hours or even days) is still limiting the  $\text{WO}_3$ -based photochromic window development [9,13]. That is why, while in the field of smart windows many researchers studied the electro/thermo-chromism of  $\text{WO}_{3-x}$  based coating, there are only a few reports on the photochromism deployment of  $\text{WO}_{3-x}$  in the same field [3]. Wootthikanokkhan *et al.* studied the optical properties of polycarbonate (PC) reinforced with  $\text{WO}_3$  nanoparticles and found that the  $\text{WO}_3$  particles, dispersed in polymer composite films, could behave as both the NIR absorptive and NIR reflective materials, depending on the illumination conditions. However, after 40 min of exposure to sunlight, the NIR absorbance of the materials increased but the bleaching was very long about 72 hours to return to the initial state [14]. In another work by Gao *et al.* [15], they reported the preparation of PVA/ $\text{WO}_3$  QDs composite photochromic film by casting (QDs for

quantum dots with 2-3 nm crystallite size). The films exhibited large optical modulation (>90%) between bleached and colored states, although the bleaching time is still long (8 h). In addition, they studied the annual energy consumption of their smart photochromic windows using EnergyPlus software simulation and they found that for a warm city (Haikou, China), using their smart window could reduce electrical consumption for cooling buildings by 27.3%. However, it is important to highlight the production method of WO<sub>3</sub> QDs suspensions which requires 12 hours of dialyzing in pure water with addition of ethylene glycol as a dispersant which need to be removed later, making WO<sub>3</sub> QDs preparation a costly process. Also, no information on film thicknesses (and so the impact of the film thickness on solar modulation) and no accurate kinetic studies are joined.

In this article, we introduce a new type of photochromic smart windows consisting of window glass coated with a thin film of tungsten trioxide/polyvinyl alcohol (WO<sub>3-x</sub>/PVA) composites that can modify their transparency properties autonomously with incident light intensity. In this way, less light is expected to be transmitted into the building on a sunny day under intense sunlight, which reduces the need for artificial lighting and air conditioning. The study offers a complete and accurate investigation of the impact of the film deposition process and the film thickness on the photochromic performances. The first part addressed the optimization of the polymeric suspension quality and photochromic contrasts of prepared films. In this part, we deeply discuss the differences in the photochromic efficiency between two series of films issued from the two adopted methods of fabrication (dip-coating and solvent coating) through multiple theoretical and experimental means. Additionally, our research offers a complete photochromic study (coloring and bleaching kinetic laws are extracted from transmission evolution versus time) with associated detailed mechanism, which is rarely reported in previous papers of the same topic

(photochromic smart windows). Also, we discuss both the photochromic and the thermal insulation properties of our prepared smart windows. It is shown that solvent-casted films (very low cost and easy-to-implement process) exhibit some adequate photochromic contrasts (colored state/bleached state contrasts) and kinetics, and act as efficient thermal barriers, with performances near to current state-of-the-art [16,17].

## **2. Materials and methods**

### **2.1. Polyol synthesis of WO<sub>3</sub> powders**

Chemical reagents were purchased from Sigma Aldrich and used as received. Tungsten (VI) chloride was used as a tungsten source and diethylene glycol (DEG) as a solvent. The WO<sub>3</sub> was synthesized by the polyol method as reported in our last paper [11] Polyvinyl alcohol (PVA) 80% hydrolyzed was used as the polymeric matrix.

### **2.2. Preparation of WO<sub>3-x</sub>/PVA coating suspension**

Firstly, a 10 wt% transparent PVA solution was prepared by dissolving PVA (80% hydrolyzed) in DI water at 25 °C under stirring for 5 h. Then, the as-synthesized WO<sub>3-x</sub> nanopowders were added to the prepared PVA. The mixtures were stirred at 500 rpm for 30 min, and then agitated strongly using a stirring bar at 1000 rpm for 1 h to gain the homogeneous WO<sub>3-x</sub>/PVA suspension.

### **2.3. Preparation of WO<sub>3-x</sub>/PVA films**

The plastic films were prepared using solvent casting (SC) and dip coating (DC) methods. For the DC method, the WO<sub>3-x</sub>/PVA suspensions were dip-coated on a standard glass substrate to obtain WO<sub>3-x</sub>/PVA composite thin films. The dip-coating parameters are (i) the dip-coating speed: 133 mm.min<sup>-1</sup> and (ii) the number of successive coating steps to produced multilayers. In

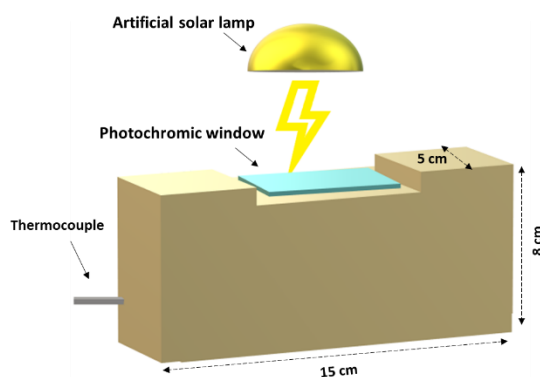
this case a 30 min drying is operated between each step in an oven (75 °C). In the case of the SC method, different quantities of the suspension were dried in the dissolved PVA plastic substrates for 1 day at room temperature then the films were peeled off and kept for post-characterization.

### **3. Characterization techniques**

Dynamic light scattering (DLS) was used to determine the size distribution profile of the pristine and doped NPs in the suspensions used for the dip coating process with a VASCO<sup>TM</sup> nanoparticle size analyzer. A real-time signal was measured; acquisitions were implemented every 30 s if the noise of the signal did not exceed 1.06%, and 8 acquisitions were accomplished during 16 min. Size distributions of the nanoparticles in PVA were analyzed by the Cumulant algorithm (assuming monodisperse dispersion), provided by NanoQ software. Assuming the small quantity of PVA fraction in our suspensions (10 wt%), we have used the refractive index of water as a reference ( $n=1.333$ ) to conduct all measurements. The acquisition temperature for all measurement was fixed automatically by the device at 20°C.

Films Transmission spectra were recorded at room temperature from 200 to 2500 nm on a Cary 5000 spectrophotometer. The irradiation conditions were accomplished using a UV Hg lamp (Vibert Lourmat 8. LC) at a monochromatic wavelength of 365 nm. The film was placed at 10 cm from 8 W tubes: the power per surface unit received by the sample is equal to 5.6 W/m<sup>2</sup>, i.e. irradiance close to the UV-daylight irradiance in London daylight. The use of such low fluence is to mimic the real condition in a smart device (window or textiles) that is exposed to daily light. Self-bleaching occurred naturally after samples were placed in a dark room. The thickness of the films was determined using a WYCO NT1100 optical profilometer for the DC films and a Dektak 32-6M Stylus for the

SC films. Finally, a prototype room was designed and fabricated to study the actual thermal isolation effect of our films. The room is a cuboid, the length, width, and height (external dimensions) are 15 cm, 8 cm, and 5 cm, respectively, and the thickness of each wall is 1.2 cm. The room has one top window, which is centered on the corresponding surface. The window size is 4.5 cm wide and 5 cm high. The window is equipped with a 2.5 mm ordinary glass or photochromic glass and a thermocouple placed in the middle of the room to record in real-time the evolution of the inner temperature under irradiation of a solar simulator (Sol1An, Newport) with an AM 1.5 spectrum as illustrated in scheme 1. The irradiance received by the window has been set at  $100 \text{ mW/cm}^2$  with a calibrated silicon radiometer (Oriel P/N 91150V).



*Scheme 1: The modeled room for thermal isolation measurements.*

### **3. Results and discussions**

#### **3.1 Suspension studies**

To tune the PVA matrix uptake percentage in the 30 mL aqueous suspension of the as-prepared blue  $\text{WO}_{3-x}$  nano-powders (NPs) from the polyol process, a fixed concentration of  $6.5 \text{ g.L}^{-1}$  for the  $\text{WO}_{3-x}$  particle was mixed with different weight percentages of the PVA dispersant (0, 1, 2, 3, 4, 5, 10 wt%), as shown in the photograph reported in Fig.1a (inset). It shows a progressive

change of color from highly turbid blue suspension to light transparent blue with the increase of the PVA content. Indeed, the higher the dosage of the PVA, the more transparent the film is until the colloidal suspension color stabilizes in 5-10% of PVA. DLS measurements were used to track the size variation of the 6.5 g.L<sup>-1</sup> dispersed NPs as a function of the PVA dose. A remarkable decrease in the average size given here in number-based (*volume-based diameter can be added also for information*) was observed once using the PVA dispersant as revealed in Fig.1a. The average size drops from 442 nm in 0% PVA to 62 nm (*109 nm volume –based diameter*) in 1% PVA until it reaches the size of almost 10 nm (*21 nm*) in the 5 or 10% PVA sample. The PVA plays a dual role in the polymeric suspension as a polymer matrix (in the way, after the suspension drying, WO<sub>3</sub> – PVA polymeric-matrix composites could be obtained) and dispersant for the WO<sub>3-x</sub> NPs aqueous suspensions. Obviously, WO<sub>3</sub> NPs surface, with a zeta potential about -40 mV at pH about 6 [13] from a PCN value about 1.5, water is already without the use of PVA the most adequate dispersing medium for such nanocolloidal suspension preparation. Table 1 summarize the values of mean size and the polydispersity index (PDI) (defined as the standard deviation ( $\sigma$ ) of the NPs diameter distribution divided by the mean NPs diameter) for all samples.

Table 1: Summary of the mean size and PDI of the studied series.

<b>PVA (wt%)</b>	<b>Mean size (number-based)</b>	<b>PDI</b>
<b>0</b>	442 ± 15 nm	0.65
<b>1</b>	62 ± 12 nm	0.35
<b>2</b>	29 ± 3.5 nm	0.32
<b>3</b>	22 ± 1.5 nm	0.22
<b>4</b>	16 ± 1.9 nm	0.21
<b>5</b>	10 ± 2.2 nm	0.25
<b>10</b>	9 ± 1.4 nm	0.13

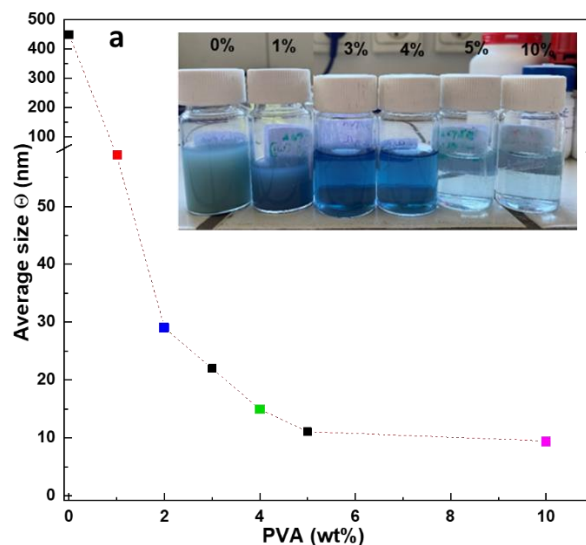


Figure 1: a) Evolution of the average NPs size as a function of the PVA weight percentage. Inset: photograph of the as-prepared PVA/WO<sub>3-x</sub> suspensions.

Furthermore, the light transmission of the suspension series was measured into a quadrate optical cuvette with a 1 cm path length. It was already reported in previous work that the oxygen sub stoichiometric WO<sub>3-x</sub> NPs as-prepared from polyol process are absorbing UV range due to O<sup>2-</sup> → W<sup>6+</sup> transfer (wide band gap semiconducting properties) and exhibits a Gaussian absorption band due to the W<sup>5+</sup> → W<sup>6+</sup> intervalence charge transfer (IVCT) in the near-infrared region (band centered at about 1,2 μm). A transparency window can so be reached in the visible part of the spectrum while the IVCT band can be modulated in intensity from UV irradiation, which is at the origin of the photochromic activity [13,18]. In the visible range, the suspension transparency improved as the average particle size decreased or the PVA charging dose increased, Fig.2a. In addition, the suspension with lower than 3% PVA almost loses NIR transmittance modulation ability. The 1 or 3% PVA suspensions exhibit a very low transmittance in the near-infrared range, i.e. for wavelengths for which the photochromism takes place. On the contrary, the 5 or 10% PVA suspension shows the largest optical modulation potentiality in the infrared region

thanks to their very low turbidity. Thus, it appears that suspension turbidity due to the particle scattering phenomenon has to be limited to optimize the suspension photochromism.

To evaluate the impact of the PVA dispersion efficiency on the particle size in the studied series, a simulation of the optical transmittance using the Mie calculator software was carried out as illustrated in Fig 2.b in parallel to the experimental data. When a beam of light propagates into a medium, the beam will be attenuated and the transmittance can be calculated following the equation:  $T = e^{-(TAC * l)}$ , where  $TAC$  is the total attenuation coefficient, and  $l$  is the thickness of the scattering medium ( $l$  is so fixed to 1 cm, the path length of the quadrat optical cuvette, for direct comparison of the simulated and the experimental measurements). The TAC value can be obtained through the Mie scattering calculator program. In addition to various important parameters: sphere diameter ( $d$ ), wavelength (calculation has proceeded for monochromatic irradiation), index of refraction of the dispersive medium, real and complex refractive indexes of the  $WO_3$  colloidal spheres, and particles concentration (number of spheres per cubic micron,  $C = N_{part}/V_{medium}$ ) [19]. Rigorously simulating the colloidal suspension turbidity faces a complex issue since the suspension offers different scattering interfaces:  $WO_3$ -water,  $WO_3$ -PVA, and PVA-water, and potential multi-scattering phenomena. As PVA macromolecules gets an efficient dispersing effect, it was considered that the particles are well embedded in PVA shells and so that the active scattering interface, in first approximation, is mainly the  $WO_3$  NPs – PVA shells interface. In addition, the used simulation software does not take into account, a 2-flux approximation, or multi-scattering eventualities. The real index of refraction ( $n$ ) of the  $WO_3$  spheres at different wavelengths, was extracted from literature references ( $n-WO_3 = 2.3$ ) [20]. As an additional difficulty, the exotic blue color for the as-prepared oxygen-sub stoichiometric tungsten oxide NPs are associated with the exotic  $k$  index which cannot be extracted from

literature results. Furthermore, the  $k$  complex refractive index evolves versus wavelength. That is why, the suspension turbidity simulation was performed for an irradiation wavelength of 500 nm, *i.e.* in the middle of the transparency window (far from the occurrence of both the electronic band transfer and the IVCT), where the  $k$  index can be considered nearly null. The simulated results are summarized in Fig.2b where the particle size  $d$  varies from 500 nm to 10 nm. Comparing the experimental data and the simulated data, which are almost superimposed, one can conclude that the transparency of the suspension in the visible band is directly correlated to the particle size diameter and that the average diameter of the tungsten oxide particles dispersed in solution is well efficient decrease thanks to PVA addition until 5 wt% PVA.

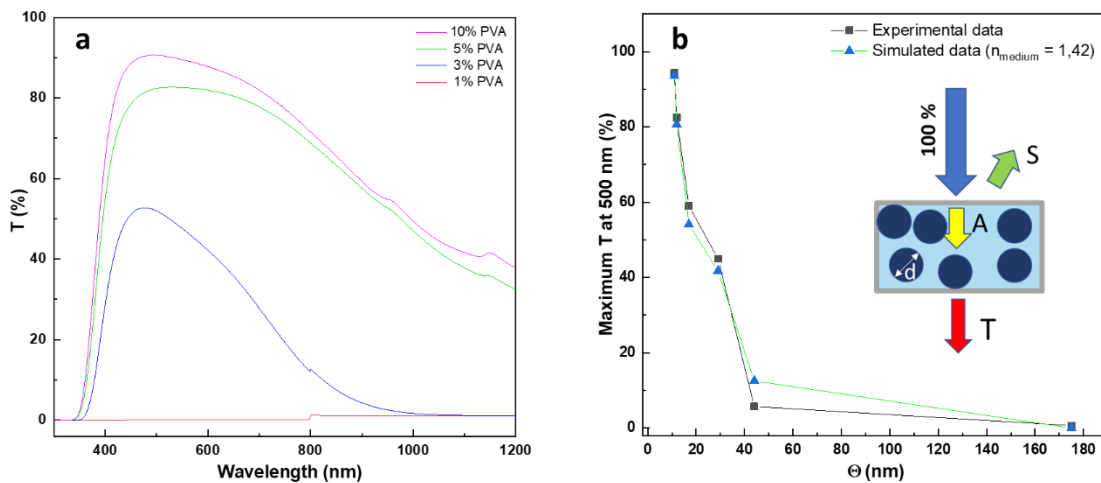


Figure 2: a) Optical transmission of different PVA/ $WO_{3-x}$  suspensions depending on the PVA wt.%, b) Comparison of the experimental transmission at 500 nm through the 1cm length cuvette and the simulated transmission at the same wavelength through the same medium thickness as a function of average particle diameter. Inset: additional schematic illustration of the simulated parameters and method.

### 3.2 From suspension to film: elaboration and optical properties

This part is devoted to the elaboration from suspension to plastic films and the characterization of its optical properties, focusing on the comparison between the films prepared from the two adopted coating processes: dip-coating (DC) and solvent casting (SC).

All samples were prepared from suspensions using the NPs concentration equal to  $65 \text{ g.L}^{-1}$ , and 5 wt. % of PVA plastic matrix, i.e. the suspensions for which best transparency was observed (previous section). The first PVA- $\text{WO}_3$  composite film series was issued from successive dip-coating steps (with 1, 2, 4, 8, or 10 successive coated layers) on glass substrates, where the number of successive coatings allows the control of the final film thickness. The second batch of films was prepared by solvent casting producing a well-controlled thickness mainly tuning the amount of the casted suspension (20, 40, 80, 100, or 130 g of the 5% PVA) on a  $2 \text{ cm}^2$  glass substrate surface. The film labels and associated thickness are listed in the table below (Table 2). Dip-coating and solvent casting processes lead to two well-separated series on the point of view of the film thickness as “sub-micrometric thin films” from 0.1 up to  $1.35 \mu\text{m}$  for the DC films, and “sub-millimetric thick films” from 100 up to  $550 \mu\text{m}$  about for the SC ones.

Table 2: Dip-coated and solvent-casted film labels and their measured associated thickness from profilometric analyses.

<i>Coating process</i>	<i>Film ID</i>	<i>Thickness (<math>\mu\text{m}</math>)</i>
<i>Dip Coating</i>	<b>D1</b>	<b>0.098</b>
	<b>D2</b>	<b>0.215</b>
	<b>D3</b>	<b>0.422</b>
	<b>D4</b>	<b>0.622</b>
	<b>D5</b>	<b>0.838</b>
	<b>D6</b>	<b>1.355</b>
<i>Solvent Casting</i>	<b>S1</b>	<b>112</b>
	<b>S2</b>	<b>180</b>
	<b>S3</b>	<b>225</b>
	<b>S4</b>	<b>356</b>
	<b>S5</b>	<b>552</b>

In their pristine state (before UV-irradiation), the transmission spectra of as-prepared thin films show a good visible and NIR transmission with a quite low scattering coefficient (Fig.3a). The DC films show a maximum transmission equal to 87 % at 600 nm (D1 sample), then decrease of this value is observed versus the film thickness increment down to 45% for the D5 sample. The D6 sample exhibits low transmittance, due to the degradation of film homogeneity quality increasing with the coating numbers. In addition, in the near-infrared region, the transmission at 1200 nm varies from 80% for the 98 nm-thick film (D1) down to 37% for the 838 nm-thick one (D5). Whereas, as shown in Fig. 3c, the SC films show a slightly lower transmission around 75% in the middle of the visible range with also degrading transparency with the increasing of the film thickness. In the NIR range, transmission value varies from 65% for the 112  $\mu\text{m}$ -thick film (S1) down to 31% only for the 225  $\mu\text{m}$ -thick film (S3). The two thicker films (S4 and S5) exhibit too low transmittance values even in their pristine state. It can be noticed that a distinct low-intensity absorption band appearing at a wavelength around 1 - 2  $\mu\text{m}$  is observed on the D5, D6, and S3 films. This absorption band can be without any doubt attributed to the presence of initial  $\text{W}^{5+}$  ions causing the intervalence charge transfer (IVCT) between  $\text{W}^{5+}$  and  $\text{W}^{6+}$  ions in the crystal network of the  $\text{WO}_{3-x}$  compound [18].

A preliminary photochromic test with fixed irradiation conditions (UV lamp with 8 W, 20 min associated with irradiation surface power of  $5.6 \text{ W}\cdot\text{cm}^{-2}$ ) has been conducted on all studied films as shown in Fig.3b and d. The irradiation affects all film optical properties, especially at the frontier between the visible and near-infrared regions, with higher activity in the near-infrared region. Indeed, the direct exposure to UV irradiation produces a pale blue coloration of the films suggesting a significant increase of  $\text{W}^{5+}$  as a result of the photo-redox process which was thoroughly studied in our previous works [11], or elsewhere in literature [20,21]. In all

elaborated films, an important loss of transmission was observed at 1200 nm while this decrease is not that obvious at 600 nm. The contrasts between colored and bleached states (contrasts between irradiated and non-irradiated states) will be independently investigated in the visible range and the NIR range and discussed in the next part.

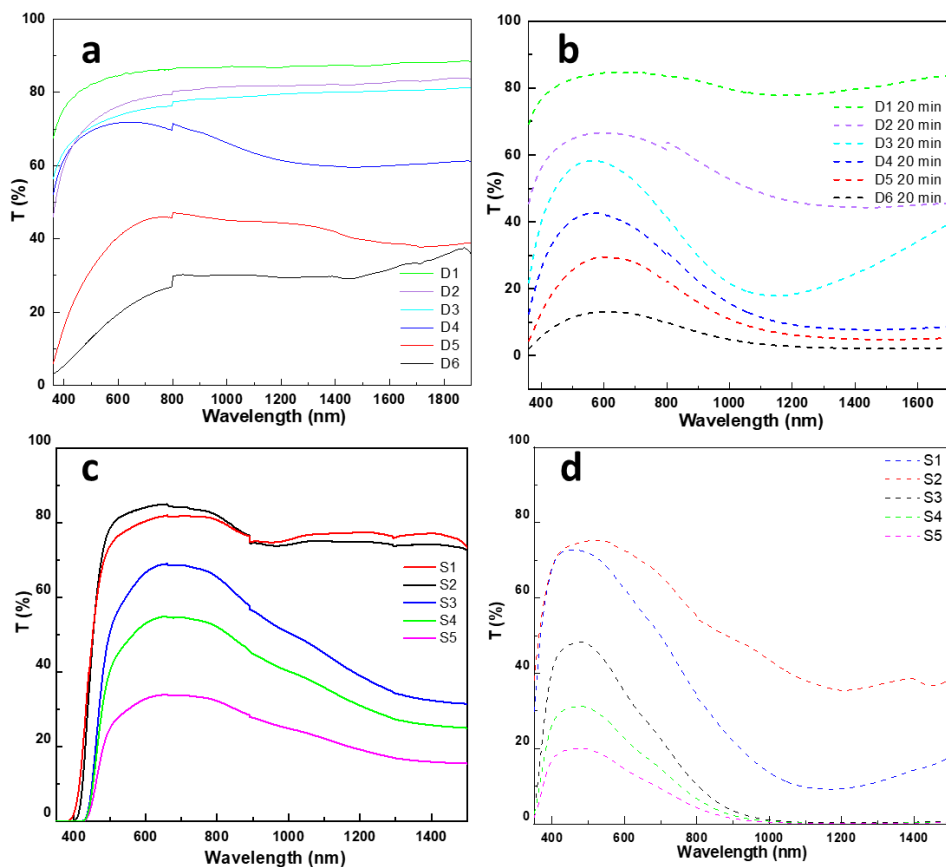


Figure 3: Transmission spectra before irradiation (in solid line) and after irradiation (in dashed line) of a, c) dip-coated films, b, d) solvent-cast films.

In the visible range, the transmission spectra allow the calculation of the associated chromatic coordinates in  $L^*$ ,  $a^*$ , and  $b^*$  space (reported in Fig.4 and Fig.5 for respectively the DC and SC samples). Indeed, even if our films exhibit a photochromic effect mainly concentrated in the near-infrared part of the spectrum, the impact of the inter-valence transfer in the visible range

allows the observation of visible “photochromic” contrast defined such as:  $\Delta C_{\text{vis}} = \sqrt{(\Delta b^{*2} + \Delta L^{*2} + \Delta a^{*2})}$ , taking into account color parameters calculated before and after the UV irradiation. The visible contrasts allow the comparison of the photochromic efficiency of the samples issued from both coating processes. In the near-infrared, where the photochromic efficiency is the highest in terms of transmittance modulation, such an “optical contrast” cannot obviously be extracted. Thus, we proposed an infra-red optical contrast ( $\Delta T_{\text{IR}}$ ), calculated as the average transmission difference in the range 800 nm up to 2500 nm, between the two states (non-irradiated and irradiated states) of each film (what can be seen as the area difference between the two transmission curves corresponding to the pristine and irradiated state in the whole NIR region).

The evolution of both  $\Delta C_{\text{vis}}$  and  $\Delta C_{\text{IR}}$  are reported in Fig. 4 and 5, respectively for the DC samples and the SC samples. For both film series, bell shape curves are obtained for the visible contrast as well as for the NIR contrast, meaning an optimal film thickness is reached in both cases. This result can appear as surprising since the two series differ greatly in terms of thickness. At this stage, only hypotheses can be proposed. The degradation of the contrasts with increasing the film thickness can be produced: (i) either by scattering phenomena (which can be linked to film homogeneity degradation as the inclusion of pores in between the successive coated layers of the DC series, for illustration); (ii) or by too large light absorption through films (while an equivalent thickness of  $\text{WO}_3$  powder becomes too high for the thicker films as for the last samples of the SC series, for illustration). The maximal values of the  $\Delta C_{\text{vis}}$  and  $\Delta C_{\text{IR}}$  are 34.37 and 7.9, which were recorded for the S2 and S3 films, respectively; whereas  $\Delta C_{\text{vis}}$  and  $\Delta C_{\text{IR}}$  reached less than 20.2 and 5.4 for the best films issued from the DC process (D4 and D5). Hence, the casted films, exhibit the best photochromic amplitude despite a large thickness thanks

to the conservation of a highly visible and still moderate NIR transparency. SC films are also the most promising for their use as solar filters, *i.e.*, with the best contrast between visible and near-infrared transmission, especially in their irradiated state. At this stage, it can be supposed that the SC process, which is a “one step” coating process, preserves composite films homogeneity regarding the DC process, which leads to the degradation of films homogeneity from the inclusion of pores, inhomogeneity, or other defects in between layers during the successive coating operations.

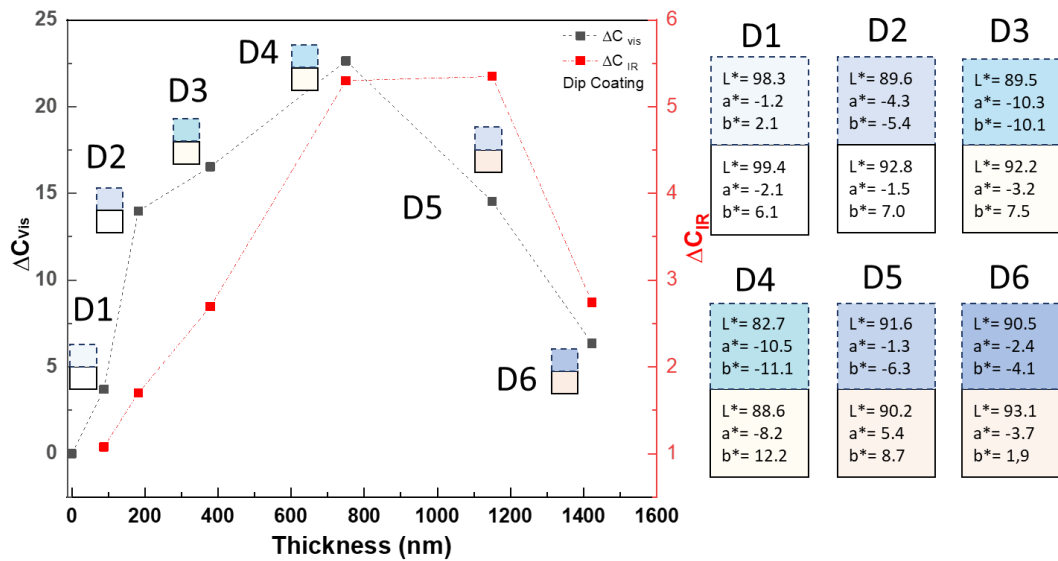


Figure 4: Calculated optical and infrared contrasts of DC films as a function of their thickness and their associated  $L^*$ ,  $a^*$ ,  $b^*$  parameters before irradiation (solid line) and after 20 min UV irradiation (dashed line).

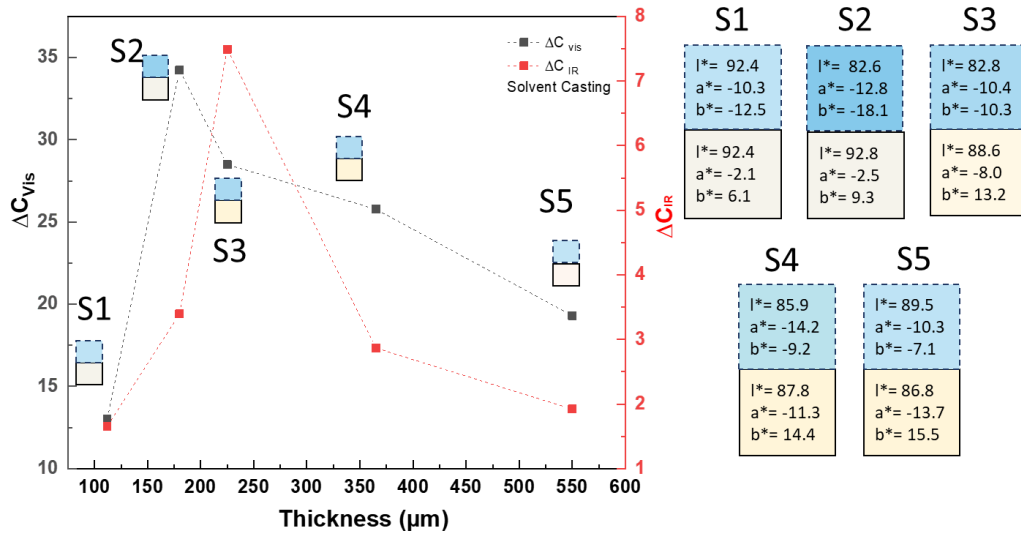


Figure 5: Calculated optical and infrared contrasts of SC films as a function of their thickness and their associated  $L^*$ ,  $a^*$ ,  $b^*$  parameters before irradiation (solid line) and after 20 min UV irradiation (dashed line).

The previous method did not give clear information about the role of absorption versus the scattering of the NPs particles in the total transmission loss. Thus, another theoretical model was investigated to disentangle the associated impacts of absorption and scattering in our plastic films.

The absorption and scattering coefficients of all the scattering centers (tungsten oxide NPs dispersed in the PVA polymeric medium) characterize the composite film's optical properties. The light diffusion theory can help us to predict the visual appearance of layers composed of  $WO_{3-x}$ /PVA composite. The absorption and scattering properties of the scattering centers are described by the radiative transfer equation (RTE). Both are important to simulate the incoherent light propagation inside the medium [22,23] The simplest method of solving the RTE is the two-flux method (Kubelka–Munk) model [24]. In this model: only two diffuse fluxes with opposite directions but both normal to the interfaces are taken into account, also it is supposed that the two fluxes are isotropic. The studied medium is characterized by the absorption and scattering extrinsic coefficients  $K(\lambda)$  and  $S(\lambda)$ , which are related to the intrinsic ones  $k(\lambda)$  and  $s(\lambda)$  by the

following equations:  $K(\lambda)=2k(\lambda)$  and  $S(\lambda)=s(\lambda)$ [22]. To apply the 2-flux model, one has to perform the calculation considering the composite film thickness:  $h$ , which is coated on an opaque and reflective background characterized by its reflectance factor  $\rho_g$ . At a given wavelength, the flux balance can be written and then integrated over the whole thickness  $h$  to give the reflectance factor  $\rho$  of the composite films, (more details about the integration and deducing of the final equation are discussed in the references [24,25]):

$$\rho = \frac{1-\rho_g[a-b \coth(bSh)]}{a+b \coth(bSh)-\rho_g} \quad \text{Equation 1}$$

Where  $a = (K+S)/S$ , and  $b = (a^2-1)^{1/2}$ .

To determine  $S(\lambda)$  and  $K(\lambda)$ , two experimental sample series to get two different equations are required: one sample coated on an opaque black background (with reflectance:  $\rho_{g1}$ ) and another sample coated on white one (reflectance:  $\rho_{g2}$ ). By measuring the reflectance factors of both samples ( $\rho_1$  and  $\rho_2$ ) coated respectively on both backgrounds ( $\rho_{g1}$  and  $\rho_{g2}$ ),  $S(\lambda)$  and  $K(\lambda)$  are determined for each wavelength in the range 0.3-2  $\mu\text{m}$ , thanks to equation 1. The four experimental inputs (the four measured reflectance spectra) are presented in Fig.6a. The output data was obtained using Wolfram Mathematica software, an example of two diverging results, comparing the cases of the S2 thick SC film and the D4 thin DC film is shown in Fig.6b, where the absorption factor is higher than the scattering factor for S2, meaning that absorption dominates and therefore the reflectance factor is low, whereas the reverse is observed for D4. Furthermore, it can be seen, as predicted from Mie scattering theory [26], that the  $S$  parameter tends to decrease versus wavelength. This can clarify why the best  $\Delta C_{\text{vis}}$  are reached for the thinner thickness with the best  $\Delta C_{\text{IR}}$ , for both series, i.e. the scattering/absorbance ratio decreases with wavelength, and the deterioration of the visible contrast is more quickly visible than the deterioration of the infrared contrast. The maximum  $S(\lambda)$  and  $K(\lambda)$  factors are summed up in

Fig.6c and 6d, respectively, as a function of the thickness of both DC and SC films series. As we can notice, the absorption factor increases as the thickness of the film increase for both coating methods (DC and SC). Furthermore, proportionally to their thickness, thick SC films exhibit larger K coefficients than DC thin films. In contrast, the scattering factor is higher in the case of the DC reaching the value of  $58 \text{ cm}^{-1}$  compared to  $28 \text{ cm}^{-1}$  in the SC films. This last observation confirms that porosity or dust as additional scattering factors should be introduced in the case of DC films because of the multi-coating aspect of the DC process. From the theoretical and experimental detailed study of the film's optical properties, one can conclude that the SC method offers films that are better candidates for optical application in terms of scattering reduction, improved visible/infra-red contrast, and better photochromic efficiency thanks to a higher absorption strength.

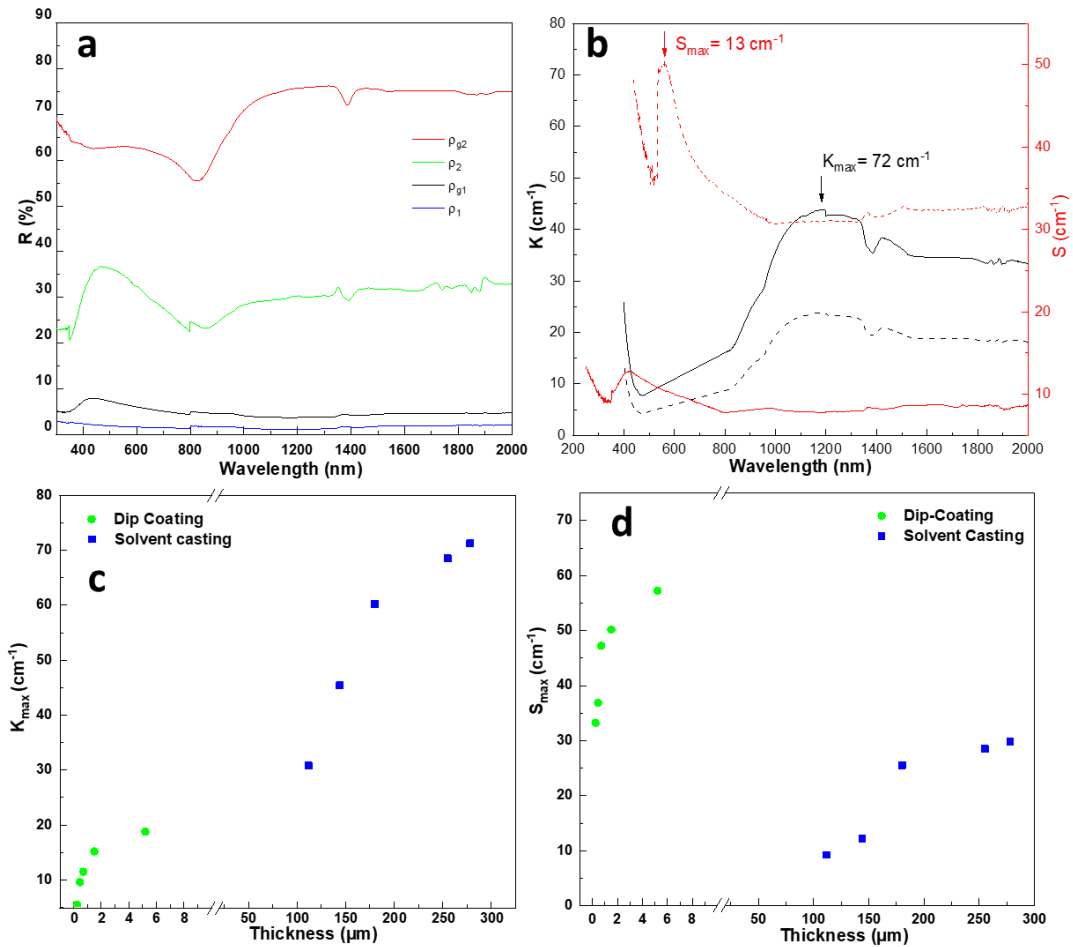


Figure 6: a) The four reflection spectra as inputs in the two flux model, b) one example of the final output  $S(\lambda)$  and  $K(\lambda)$  using the S2 (solid line), D4 (dashed line) films as an example, c) the  $K_{max}$  and d)  $S_{max}$  for all studied films as a function of the thickness.

### 3.3 Photochromic properties of the films:

In these measurement series, a focus was made on the 665 nm (DC) (D4 sample) and 220  $\mu\text{m}$  (SC) (S2 sample) films since for both samples, a significant high photochromic efficiency associated with a drastic increase of IVCT transfer versus irradiation time are observed, especially in the NIR-region. These two samples were the ones in their respective series, which possess the best visible contrast and the second-best infrared contrast. The two films were

irradiated with fixed irradiation conditions (UV lamp, 8 W, 30 min, lamp-sample distance equal to 20 cm). These preliminary tests have shown that UV-irradiation well generates the photochromic coloring effect. Therefore, the evolution of the spectrum of both films versus irradiation time was collected (Fig.7a and Fig 7b). The absorbance evolution at 1.1 eV is extracted to investigate further the photo-redox kinetics (Fig.7c). The absorbance at 1.1 eV (corresponding to the energy at which the IVTC band is the maximum) of both films seems to change rapidly in the first minutes of irradiation, then it slows down beyond 20 min of irradiation until almost no longer evolving after 90 min. To better express the differences between both films, an exponential growth function (first-order kinetic law) was used to fit the experimental data (absorbance evolution at its maximum), according to the Equation 2:

$$Y(\text{“total absorbance”}) = S_0 + A_g \cdot [1 - \exp(-t/\tau_g)] \quad \text{Equation 2}$$

with  $t$  in min,  $\tau_g$  is the characteristic coloring time in min,  $A_g$  is the characteristic growth (coloring from IVCT absorbance band) amplitude and  $S_0$  is the y-offset due to scattering phenomena mostly. The values of the three parameters are shown in the inset of Fig.7c and 7f. The SC film recorded a slightly faster coloring kinetics compared to DC one (12.3 to 17.4 min). Moreover, significantly higher absorbance amplitude ( $A_g$ ) is observed for the latter, which can be attributed to the higher thickness containing multiple numbers of absorption centers as was proven by the two-flux model discussion. For both films, the coloring kinetic consists of photo-reduction of the surface cations from  $W^{+6}$  to  $W^{+5}$  until the surface becomes saturated with  $W^{+5}$  ions, and this fast mechanism slows down afterward. For the bleaching properties, the studied films that were previously irradiated for 120 min (to nearly gain the coloring saturation) and let in dark at room temperature for self-bleaching, show photochromic reversibility. The bleaching study was performed in the spectrometer chamber (dark condition) to record the evolution of the

transmission spectra: a spectrum analysis is automatically performed every hour for 20 hours, stopping the sample illumination at 500 nm to produce any electron/hole pair creation. The spectra during the self-bleaching process are recorded while avoiding re-exciting the sample from UV irradiation (spectra recorded only on visible – NIR ranges). The absorbance spectra for the bleaching half cycle are shown in Fig.7c and 7d for SC and DC films, respectively.

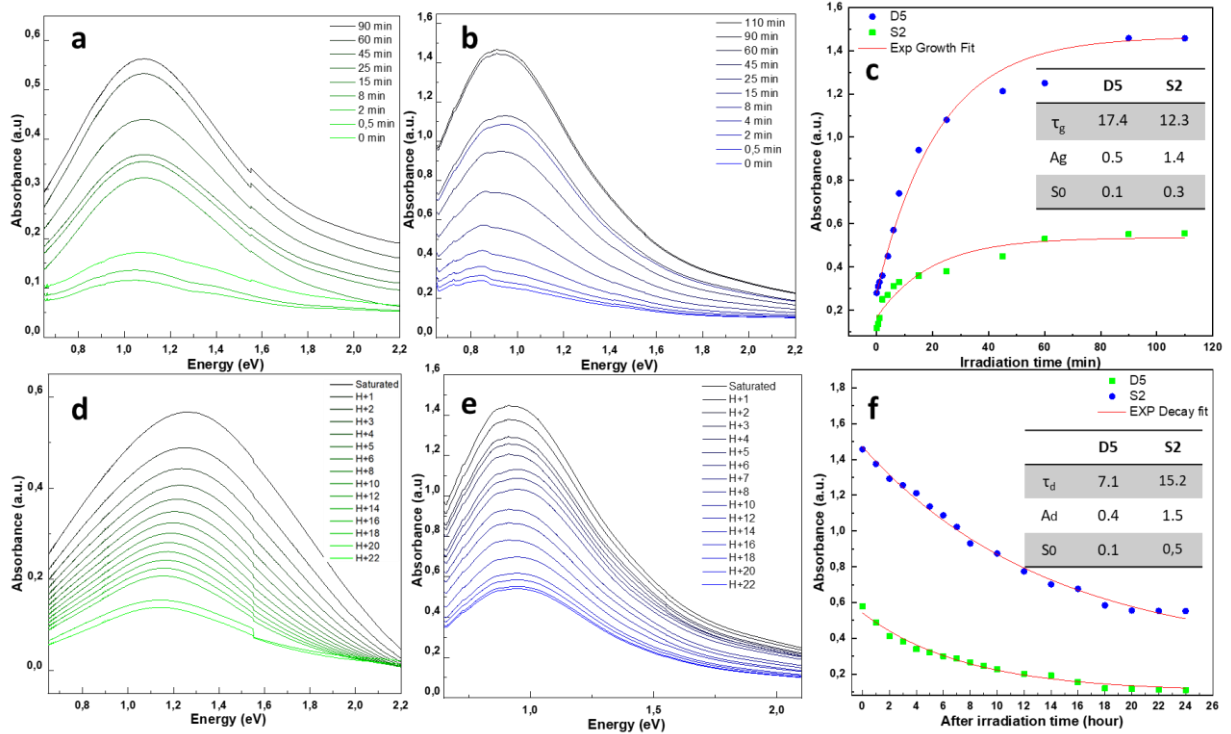


Figure 7: Evolution of absorbance during irradiation (coloring) of the D5 DC film (a), and the S2 SC film (b). For both films, absorbance at 1 eV evolution versus irradiation time and the associated kinetic parameters (coloring kinetic) (c). Evolution of absorbance in dark conditions (bleaching) of the same D5 (d) and S2 (e) films. For both films, absorbance evolution at 1 eV in dark conditions (bleaching kinetic) (f).

Similarly, to the methodology conducted to study the coloring kinetic, the bleaching evolution was followed by recording the absorbance at 1 eV. First, for the SC film, the residual absorbance at 1 eV obtained after 20 hours of darkening is still important: equal to about 0.38, whereas it is almost 0.08 in the DC film (Fig.7e). It seems that while near-full reversibility is well maintained

for the DC films, a partially non-reversible photochromism is reached for the SC films. The absorbance evolution for both films can be fitted from a single exponential decay trend on the complete 20 first-hour range. The single exponential decay function to fit the experimental data, according to the Equation 3, with  $t$  and  $\tau_d$  in hours,

$$Y = A_d \cdot \exp(-t/\tau_d) + A_0 \quad \text{Equation 3}$$

where  $A_d$  is the characteristic bleaching amplitude and  $A_0$  is the y-offset reached after 120 min irradiation. Comparing both films, the speed of the bleaching mechanism in DC is almost two times faster than for the SC film:  $\tau_d = 7.1$  and 14.2 hours, respectively. This difference is mainly governed by the deep of activated  $W^{5+}$  absorbance centers (causing the IVCT between  $W^{6+}$  to  $W^{5+}$  neighboring ions) which leads directly to a longer time to get back to the natural re-oxidation  $W^{5+} \rightarrow W^{6+}$  since the thickness in the SC films is almost three times higher than the DC one. This result confirms the fact that the PVA acts as a non-neutral function in terms of kinetic, especially in bleaching mode because the polymer matrix should soften the reoxidation possibilities. From this point of view, thin films (obtained from the dip-coating process: DC films) are more efficient than thick ones (obtained from slip casting process: SC films).

### **3.4 Thermal insulation properties**

First, we conducted a preliminary test on various films (S1, S3, and S5) to evaluate the effect of thickness on the efficiency of thermal insulation. Our designed prototype room was used as a model equipped with a  $WO_{3-x}$ /PVA/Silica photochromic window and painted in white inside (see Fig.9a). Thermal insulation performance was measured by introducing a thermocouple in the inner room and then recording the changes in temperature after irradiation under an artificial solar source lamp in real-time (Fig.8). As a reference, a virgin boro-silica window was also

tested. The measurements were conducted in a special room designed for sensing application, i.e. temperature of the room was controlled to be always at 20 °C.

Furthermore, the measurements were recorded one time with the film facing (front model) the solar source and another time with the film opposite (back model) to the solar source. Under the powerful solar irradiation used the film changes its color from transparent to blue within less than a few 10 s, i.e. very quickly regarding the recording time of the temperature evolution and that is the key (the maximum of optical modulation) to efficient thermal insulation. Indeed, it can be considered that films have reached their colored state with all the absorbance centers that will act as a thermal barrier.

In both designs (front and back), all photochromic windows successfully act as a thermal barrier and block the temperature from raising inside the room with higher efficiency compared to a virgin window without coating as shown in Fig.8 a,b. In all tested films, the front design exceeds the back one in terms of temperature difference (defined as thermal difference at the maximal temperature  $\Delta T_i = T_{\text{back/front}} - T_{\text{REF}}$ ) as shown in table 3. To better decide which film is more suitable for the post-insulation application, we calculated the difference between  $\Delta T_{\text{front}} - \Delta T_{\text{back}}$  as resumed in table 2, the S3 film has a maximum contrast equal to 6.9 (between the back and front designs) among all films which make it the best choice for post thermal application. This film can serve as a thermal barrier and regulator depending on the deposition side (front or back) with the least required materials to be fabricated.

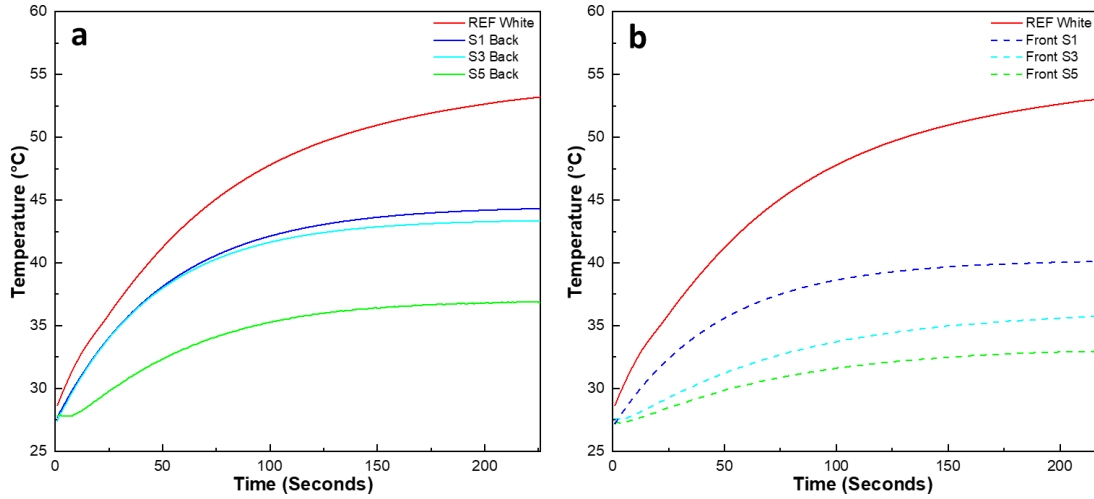


Figure 8: Temperature-time dependent change of the inner room: b) Back design, c) Front design.

Table 3: Thermal difference parameters extracted from Fig.8 a,b.

<i>Film ID</i>	$\Delta T_{back}$	$\Delta T_{front}$	$\Delta T_{front} - \Delta T_{back}$
<i>S1</i>	<b>11.5</b>	<b>13.3</b>	<b>1.8</b>
<i>S3</i>	<b>12.6</b>	<b>19.5</b>	<b>6.9</b>
<i>S5</i>	<b>19</b>	<b>23</b>	<b>4</b>

As the thermal efficiency was tested under coloring mode, the S3 film was chosen to test the thermal insulation behavior. Two wooden room designs were adopted: one using a white-painted inner room and the second one with a black one. Six measurement series are so executed (white ref and black ref are for the measurements that were made on a white and black-painted box with the standard window series, and white-front, black-front, white-back, and black-back addressed the four experimental combinations) to find the best design for this application. To better quantify the photo-thermal behavior of the film, the temperature-time curves were modeled using a bi-exponential model for each segment alone (i.e., during solar irradiance exposure for the first segment, and natural cooling down after stopping solar exposure for the second segment):

$$Y(t) = \begin{cases} T0 + Ag \cdot (1 - e^{-t/\tau_g}) & t \leq tc \\ T0 + Ag \cdot (1 - e^{-(t-tc)/\tau_d}) \cdot e^{-tc/\tau_g} & t > tc \end{cases} \quad \text{Equation 4}$$

$Y(t)$  is the temperature at a given time,  $T0$  is the starting temperature at which the experiment starts.  $Ag$  is the growth amplitude of the first exponential segment (we have supposed that the growth and decay amplitude are the same since the reversibility will be total because of that the inner box will be well equilibrated after a long time, with the exterior ambient temperature which did not undergo any variation).  $tc$  is the offset time between exponential growth and decay.  $\tau_g$  is the exponential growth term (irradiation is ON) and  $\tau_d$  is the exponential decay term (irradiation is OFF). From the bi-exponential curve fits shown in Fig.9b and 9c, we obtained the fitting parameters listed in Table 4.

Table 4: Summary of the fitting parameter results using the bi-exponential function.

<i>ID</i>	<i>T0</i>	<i>Ag</i>	$\tau_g$ (s)	$\tau_d$ (s)	$\Delta T_{back}$	$\Delta T_{front}$
<i>REF White</i>	<b>28.7</b>	<b>24.7</b>	<b>80.3</b>	<b>85.6</b>	-	-
<i>REF Black</i>	<b>32.6</b>	<b>23.2</b>	<b>107.6</b>	<b>96.5</b>	-	-
<i>White Front</i>	<b>27.5</b>	<b>7.1</b>	<b>58.6</b>	<b>89.6</b>	-	<b>19.5</b>
<i>White Back</i>	<b>28.1</b>	<b>12.5</b>	<b>62.3</b>	<b>74.7</b>	<b>12.6</b>	-
<i>Black Front</i>	<b>31.2</b>	<b>6.8</b>	<b>53.8</b>	<b>106</b>	-	<b>20.2</b>
<i>Black Back</i>	<b>31.9</b>	<b>10.2</b>	<b>71.0</b>	<b>115</b>	<b>15.5</b>	-

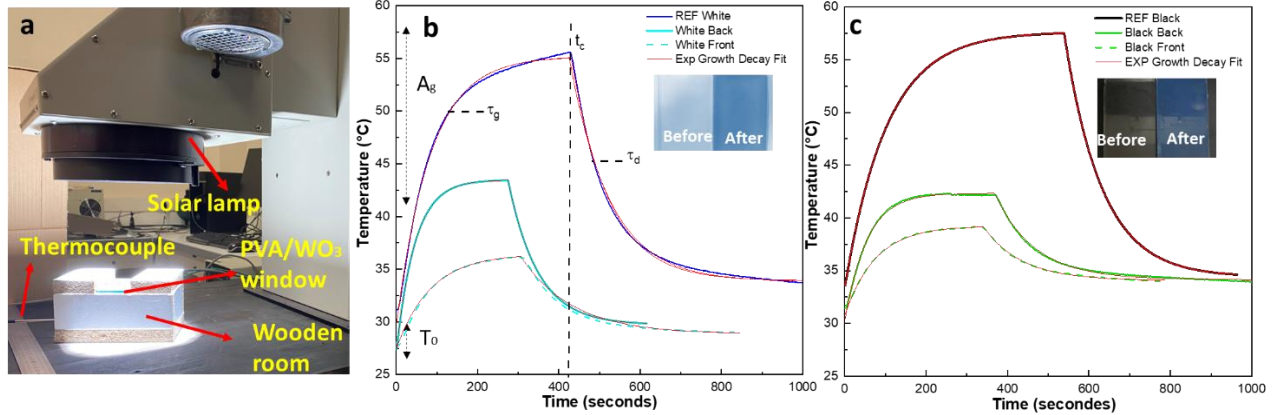


Figure 9: a) Photograph of our room design equipped with the smart window coated PVA/WO<sub>3</sub>, Temperature-time dependent change of the inner room: b) white model, c) black model (with photographs of each smart window before and after irradiation).

With the standard (virgin) glass window, the heating amplitude is about 24°C for both black and white boxes. Surprisingly, the equilibrium temperature is not significantly impacted by the inner color of the wooden room. The white and black room designs and both models (front and back) provide very good thermal insulation properties compared to the reference, which was also recorded in the same conditions. The front model in both designs (black and white) gives a superior thermal difference at the maximal temperature: in the case of the white room the  $\Delta T_{\text{front}} = 19.5$ , compared to  $\Delta T_{\text{back}} = 12.6$  for the back model. In the black-painted room, the thermal insulation properties were almost the same as the white room design with a  $\Delta T_{\text{front}} = 20.2$  and  $\Delta T_{\text{back}} = 15.5$ . These results confirmed that the inner paint color does not affect the thermal equilibrium of the system (room and window) which means that our films offer a feasible performance no matter what is the color of the inner wall (black or white). As revealed from the fitting parameter, the growth time is lower than the decay time in both designs (black and white) which was expected since the decay phase takes more time to reestablish the thermodynamic balance with the exterior atmosphere. The black model requires more time to come back to its initial state due to its color that can absorb part of the heat adding more time to reach the balance

again. Table 5 summarizes the performance of various based photochromic films reported in literature. The obtained photochromic windows exhibit a comparable performance when compared to many of the previous reports on such properties on other systems. Also, taking into account the simplicity of film fabrication and materials consumption one can conclude that our films offer supplementary superior economic/performance properties. The smart window design proved to be an efficient future solution for energy-saving applications.

Table 5: The performance of the current films and those reported.

<i>Materials</i>	<i>Fabrication method</i>	<i>X-chromic effect</i>	<i>Photoresponse time/wavelength</i>	<i><math>\Delta T</math> (<math>^{\circ}\text{C}</math>) <math>T_{REF}-T_{Room}</math></i>	<i>Ref.</i>
<i><math>\text{VO}_2/\text{Graphene}/\text{Cu}/\text{PET}</math></i>	<i>CVD+sputtering +Etching</i>	<i>Thermochromic</i>	<i>30 min, artificial sunlight</i>	<i><math>\Delta T=64-38=26</math></i>	<i>[27]</i>
<i><math>\text{WO}_3/\text{Quantum dots}/\text{PVA}</math></i>	<i>Casting &amp; molding</i>	<i>Photochromic</i>	<i>1 min, 365 nm</i>	<i><math>\Delta T= 47-32=15</math></i>	<i>[15]</i>
<i><math>\text{V}_{0.8}\text{W}_{0.2}\text{O}_2@\text{SiO}_2+</math> <i>(PNIPAm) microgel</i></i>	<i>Sol-gel</i>	<i>Thermochromic</i>	<i>8 min, 0.1 W.cm<sup>-2</sup> infrared lamp</i>	<i><math>\Delta T= 49-34=15</math></i>	<i>[28]</i>
<i><math>\text{WO}_{3-x}/\text{PVA}</math></i>	<i>Solvent casting</i>	<i>Photochromic</i>	<i>53 seconds artificial sunlight</i>	<i><math>\Delta T= 56-36=20</math></i>	<i>Our work</i>

## Conclusion

Effective thermal insulation has been achieved using the as-prepared composite smart windows by solvent casting method. In these films,  $\text{WO}_{3-x}$  nanoparticles ensure the role of the photochromic centers, and the PVA matrix is used as transparent polymer matrix as well as an efficient dispersing agent of the tungsten oxide colloids. A simple two-flux model (Kubelka Munk theory) was applied to track the correlation of the absorption and scattering coefficients in both adopted methods to fabricate composite films: solvent casting and dip coating processes. The calculations revealed the increase of the K absorption coefficient versus the thickness of the films while the S scattering coefficient was higher in the case of the DC method, even if DC

films are thinner than SC films. Thus, simulated and experimental data proved that the SC method has superior advantages over DC including less scattering and higher absorption so higher photochromic efficiency (i.e. higher photochromic contrast between colored and bleached states). As a first novelty, from easy-scalable, eco-friendly and quite low cost process, SC films exhibit a very high transparency in regard of the equivalent thickness of  $\text{WO}_3$  intercepting light propagation, i.e. in regard to the ability of the films to modulate the infrared transmission with the photochromic effect (high contrast between colored and bleached states). The photochromism (coloring/bleaching) kinetics of both these composite series (SC and DC) was thoroughly studied. On this aspect, thin DC films exhibit a bit superior photochromic speed than SC films, surely due to a photo-redox reaction blocking effect from the PVA matrix. In addition, the thermal insulation measurements, performed on the SC film series, indicated a very good thermal regulation performance of our smart windows, especially when the smart films are deposited on the front side of the window glasses beside the irradiation source. With this front size design, white or black-painted model rooms are well thermally insulated, with a gain of temperature moderation compared to a virgin glass window of almost  $\Delta T = 20.2$  and  $19.5^\circ\text{C}$  respectively, with white or black room design. Such good thermal insulating properties, on a passive system (photochromic system), with kinetics adequate to building window requirements (the bleaching would be completed along the night-time), represents the second main advancement of this work. This study is proof of the promising usability of our smart windows in the field of energy-saving materials and thermal insulating smart windows for the next generation of buildings.

### **Acknowledgment**

We acknowledge the support from the LIGHT S&T Graduate Program (PIA3 Investment for the Future Program, ANR-17-EURE-0027)".

## References

- [1] S. Abolhosseini, A. Heshmati, J. Altmann, A Review of Renewable Energy Supply and Energy Efficiency Technologies, 2014. <https://EconPapers.repec.org/RePEc:hhs:cesisp:0374>.
- [2] A. Allouhi, Y. el Fouih, T. Kousksou, A. Jamil, Y. Zeraoui, Y. Mourad, Energy consumption and efficiency in buildings: current status and future trends, *J Clean Prod.* 109 (2015) 118–130. <https://doi.org/10.1016/j.jclepro.2015.05.139>.
- [3] C.G. Granqvist, Oxide-based chromogenic coatings and devices for energy efficient fenestration: Brief survey and update on thermochromics and electrochromics, *Journal of Vacuum Science & Technology B, Nanotechnology and Microelectronics: Materials, Processing, Measurement, and Phenomena.* 32 (2014) 060801. <https://doi.org/10.1116/1.4896489>.
- [4] R. Pardo, M. Zayat, D. Levy, Photochromic organic–inorganic hybrid materials, *Chem Soc Rev.* 40 (2011) 672. <https://doi.org/10.1039/c0cs00065e>.
- [5] Y. Badour, V. Jubera, I. Andron, C. Frayret, M. Gaudon, Photochromism in inorganic crystallised compounds, *Optical Materials: X.* 12 (2021) 100110. <https://doi.org/10.1016/j.omx.2021.100110>.
- [6] G.P. Smith, Photochromic glasses: Properties and applications, *J Mater Sci.* 2 (1967) 139–152. <https://doi.org/10.1007/BF00549573>.
- [7] F. Corà, M.G. Stachiotti, C.R.A. Catlow, C.O. Rodriguez, Transition Metal Oxide Chemistry: Electronic Structure Study of  $\text{WO}_3$ ,  $\text{ReO}_3$ , and  $\text{NaWO}_3$ , *J Phys Chem B.* 101 (1997) 3945–3952. <https://doi.org/10.1021/jp963724z>.
- [8] C.G. Granqvist, Electrochromics for smart windows: Oxide-based thin films and devices, *Thin Solid Films.* 564 (2014) 1–38. <https://doi.org/10.1016/j.tsf.2014.02.002>.
- [9] S. Cong, F. Geng, Z. Zhao, Tungsten Oxide Materials for Optoelectronic Applications, *Advanced Materials.* 28 (2016) 10518–10528. <https://doi.org/10.1002/adma.201601109>.
- [10] J.-B. Lee, H.-J. Lee, S.-H. Seo, J.-S. Park, Characterization of undoped and Cu-doped ZnO films for surface acoustic wave applications, *Thin Solid Films.* 398–399 (2001) 641–646. [https://doi.org/10.1016/S0040-6090\(01\)01332-3](https://doi.org/10.1016/S0040-6090(01)01332-3).
- [11] Y. Badour, S. Danto, C. Labrugère, M. Duttine, M. Gaudon, Cu-Doped and Un-Doped  $\text{WO}_3$  Photochromic Thin Films, *J Electron Mater.* 51 (2022) 1555–1567. <https://doi.org/10.1007/s11664-021-09389-3>.
- [12] N. Li, Y. Zhao, Y. Wang, Y. Lu, Y. Song, Z. Huang, Y. Li, J. Zhao, Aqueous Synthesis and Visible-Light Photochromism of Metastable  $h$ - $\text{WO}_3$  Hierarchical Nanostructures, *Eur J Inorg Chem.* 2015 (2015) 2804–2812. <https://doi.org/10.1002/ejic.201500132>.
- [13] M. Bourdin, G. Salek, A. Fargues, S. Messaddeq, Y. Messaddeq, T. Cardinal, M. Gaudon, Investigation on the coloring and bleaching processes of  $\text{WO}_{3-x}$  photochromic thin films, *J Mater Chem C Mater.* 8 (2020) 9410–9421. <https://doi.org/10.1039/D0TC02170A>.
- [14] T. Sangprasertsuk, M. Phiriyawirut, P. Ngaotrakanwivat, J. Wootthikanokkhan, Mechanical, optical, and photochromic properties of polycarbonate composites reinforced with nano-

- tungsten trioxide particles, *Journal of Reinforced Plastics and Composites*. 36 (2017) 1168–1182. <https://doi.org/10.1177/0731684417710107>.
- [15] Y. Zhu, Y. Yao, Z. Chen, Z. Zhang, P. Zhang, Z. Cheng, Y. Gao, WO<sub>3</sub> quantum dot photochromical film, *Solar Energy Materials and Solar Cells*. 239 (2022) 111664. <https://doi.org/10.1016/j.solmat.2022.111664>.
- [16] J. Liu, R. Yang, J. Zhang, Q. Tao, A. Li, Z. Liu, Y. Su, Y. Liu, Dual-function smart windows with dynamic and fast thermal response for building energy-saving/storage, *Solar Energy Materials and Solar Cells*. 249 (2023) 112048. <https://doi.org/10.1016/j.solmat.2022.112048>.
- [17] Z. He, P. Yu, J. Gao, C. Ma, J. Xu, W. Duan, Y. Zhao, Z. Miao, An energy-efficient and low-driving-voltage flexible smart window enhanced by POSS and Cs<sub>x</sub>WO<sub>3</sub>, *Solar Energy Materials and Solar Cells*. 250 (2023) 112096. <https://doi.org/10.1016/j.solmat.2022.112096>.
- [18] Bourdin, Gaudon, Weill, Duttine, Gayot, Messaddeq, Cardinal, Nanoparticles (NPs) of WO<sub>3-x</sub> Compounds by Polyol Route with Enhanced Photochromic Properties, *Nanomaterials*. 9 (2019) 1555. <https://doi.org/10.3390/nano9111555>.
- [19] S. Guan, M. Gaudon, A. Rougier, E. Duguet, E. Durand, A. Fargues, O. Viraphong, N. Penin, VO<sub>2</sub> films obtained by V<sub>2</sub>O<sub>5</sub> nanoparticle suspension reduction, *Opt Mater (Amst)*. 127 (2022) 112117. <https://doi.org/10.1016/j.optmat.2022.112117>.
- [20] L.U. Krüger, C.M. Cholant, M.P. Rodrigues, J.A. Gomez, D.M. Landarin, C.S. Lucio, D.F. Lopes, L.O.S. Bulhões, C.O. Avellaneda, Photochromism of doped and undoped WO<sub>3</sub> sol-gel films: Determination and analysis of optical constants, *Opt Mater (Amst)*. 128 (2022) 112357. <https://doi.org/10.1016/j.optmat.2022.112357>.
- [21] C. Avellaneda, Photochromic properties of WO<sub>3</sub> and WO<sub>3</sub>:X (X=Ti, Nb, Ta and Zr) thin films, *Solid State Ion*. 165 (2003) 117–121. <https://doi.org/10.1016/j.ssi.2003.08.023>.
- [22] P. Kubelka, New Contributions to the Optics of Intensely Light-Scattering Materials Part I, *J Opt Soc Am*. 38 (1948) 448. <https://doi.org/10.1364/JOSA.38.000448>.
- [23] J.L. Saunderson, Calculation of the Color of Pigmented Plastics, *J Opt Soc Am*. 32 (1942) 727. <https://doi.org/10.1364/JOSA.32.000727>.
- [24] A. Roy, R. Ramasubramaniam, H.A. Gaonkar, Empirical relationship between Kubelka–Munk and radiative transfer coefficients for extracting optical parameters of tissues in diffusive and nondiffusive regimes, *J Biomed Opt*. 17 (2012) 115006. <https://doi.org/10.1117/1.JBO.17.11.115006>.
- [25] M. Hébert, P. Emmel, Two-Flux and Multiflux Matrix Models for Colored Surfaces, in: *Handbook of Digital Imaging*, John Wiley & Sons, Ltd, Chichester, UK, 2015: pp. 1–45. <https://doi.org/10.1002/9781118798706.hdi055>.
- [26] G. Latour, M. Elias, J.-M. Frigerio, Determination of the Absorption and Scattering Coefficients of Pigments: Application to the Identification of the Components of Pigment Mixtures, *Appl Spectrosc*. 63 (2009) 604–610. <https://doi.org/10.1366/000370209788559719>.

- [27] H. Kim, Y. Kim, K.S. Kim, H.Y. Jeong, A.-R. Jang, S.H. Han, D.H. Yoon, K.S. Suh, H.S. Shin, T. Kim, W.S. Yang, Flexible Thermo-chromic Window Based on Hybridized VO<sub>2</sub> /Graphene, ACS Nano. 7 (2013) 5769–5776. <https://doi.org/10.1021/nn400358x>.
- [28] R. Zhang, B. Xiang, Y. Shen, L. Xia, L. Xu, Q. Guan, S. Tang, Energy-efficient smart window based on a thermo-chromic microgel with ultrahigh visible transparency and infrared transmittance modulation, J Mater Chem A Mater. 9 (2021) 17481–17491. <https://doi.org/10.1039/D1TA03917B>.